GEOPHYSICS, VOL. 83, NO. 2 (MARCH-APRIL 2018); P. WB97–WB108, 19 FIGS., 1 TABLE.
10.1190/GEO2017-0429.1

The effects of 3D topography on controlled-source audio-frequency magnetotelluric responses

Changhong Lin[1], Sumei Zhong[2], Esben Auken[3], Hongzhu Cai[3], Handong Tan[4], Miao Peng[4], and Wenxin Kong[4]

ABSTRACT

We have investigated the 3D topographic effects on controlled-source audio-frequency magnetotelluric data. Two 3D topographic models are considered: a trapezoidal-hill model and a trapezoidal-valley model. Different responses are generated, including the amplitude of the electric field, the amplitude of the magnetic field, the apparent resistivity, and phase data. The responses distorted by the 3D topography are simulated for the source located next to and on the hill/valley. Our study indicates that all electric field, magnetic field, apparent resistivity, and phase data are influenced by 3D topography, but to different extents. These topographic effects depend on the transmission-receiver-topography geometry, the transmission frequency, earth resistivity, and the roughness of the surface. The effects in the near-field generated by topography in the survey area are quite different from those in the far-field because of the existence of the source. Compared with those in the far-field zone, the magnetic field and phase data in the near-field zone are less distorted, but more distortions can be found on the electric field and apparent resistivity data over the hill and valley models. Our results also indicate that not only can the 3D topography in the receiver area lead to strong distortions, but also that at the source position can lead to strong distortions. We concluded our study by quantifying the roughness with which the topographic distortion can be ignored, setting the accepted data distortion to a maximum of 10%.

INTRODUCTION

Controlled-source audio-frequency magnetotelluric (CSAMT) surveying was originally suggested by Goldstein and Strangway (1975) and has since been widely applied to mineral exploration, hydrocarbon exploration, geothermal exploration, and engineering exploration (Lu et al., 1999). Most CSAMT field data are collected in the presence of topography. It is well-known that CSAMT data are affected by topography, but to what degree is not clear. Hence, to improve field CSAMT data interpretation, it is desirable to study the topographic effects on the data.

In the past 20 years, numerous studies focused on the study of 2D topographic effects on electromagnetic (EM) responses. However, most of these works have been for the magnetotelluric (MT) method (Wannamaker et al., 1986; Fischer, 1989; Jiracek, 1990; Schwalenberg and Edwards, 2004). More recently, Mitsuhata (2000) investigates the 2D CSAMT responses over a trapezoidal hill and Li and Constable (2007) study the effect of seafloor topography on 2D marine controlled-source EM (CSEM) responses.

Topography is naturally 3D, and this poses limits to 2D interpretation. Furthermore, nowadays, 3D modeling and inversion become more and more useful due to the rapid development of computer facilities and numerical techniques; therefore, it is possible and also necessary to quantify topography effects in a 3D environment. Baba and Seama (2002) show the MT responses of a 3D seafloor topography model. Nam et al. (2007) simulate 3D MT responses

Manuscript received by the Editor 5 July 2017; revised manuscript received 24 November 2017; published ahead of production 12 December 2017; published online 16 February 2018.
[1]China University of Geosciences (Beijing), School of Geophysics and Information Technology, Beijing, China and Aarhus University, Visiting Researcher at the Hydrogeophysics Group, Department of Geoscience, Aarhus, Denmark. E-mail: linchh@cugb.edu.cn.
[2]China University of Geosciences (Beijing), School of Geophysics and Information Technology, Beijing, China and Shanghai Investigation, Design & Research Institute, Shanghai, China. E-mail: zhongsumei3039@163.com.
[3]Aarhus University, Hydrogeophysics Group, Department of Geoscience, Aarhus, Denmark. E-mail: esben.auken@geo.au.dk; caihongzhu@hotmail.com.
[4]China University of Geosciences (Beijing), School of Geophysics and Information Technology, Beijing, China. E-mail: thd@cugb.edu.cn; pengm@cugb.edu.cn; 2010130029@cugb.edu.cn.

with topography and compared the 3D topographic effects with two dimensions. Ren et al. (2013) present an example of topographic distortions, including displacement currents on radio-frequency MT (RMT) data collected near a 3D trapezoidal hill. Hoversten et al. (2006) examine the false CSEM anomalies produced by a gentle seafloor slope. Commer and Newman (2007) show a synthetic example of the 3D inversion of marine CSEM data with topography. Sasaki (2011) simulates 3D marine CSEM responses with topography and discusses the topographic effects in deep- and shallow-water environments. Wirianto et al. (2011) show an example, in which the effect of surface topography is shown not to destroy the CSEM time-lapse signal on land using the airwave effect at two different low frequencies. However, reports of 3D experimental CSAMT responses involving land-topographic effects are rarer than marine topography studies. Two simple examples of 3D topographic effects on CSAMT data were shown in Lin et al. (2017), but the focus was on the 3D CSAMT modeling and inversion technique. However, 3D topographic effects were not addressed in depth.

In this paper, we discuss the effects of 3D topography on CSAMT responses more thoroughly. We propose two topographic models to evaluate the effects. Based on the 3D CSAMT modeling code (Lin et al., 2017), the amplitude of the electric field $|E|$, the amplitude of the magnetic field $|H|$, the apparent resistivity ρ_s, and phase ϕ data are simulated. The resulting characteristic of the topographic responses from the numerical simulations, which to the best of our knowledge is not available in previous publications, provides new insight into the effects of land topography on CSAMT data.

METHODOLOGY

The investigated models

Trapezoidal-hill model

The trapezoidal-hill model over a uniform half-space is shown in Figure 1. The hill height (z_0) is varying. The hill is 0.03 km at the hilltop and 1.03 km at the base. An x-directed horizontal electric dipole (HED) transmitter is located at (−3.185, 0, and 0) km on the surface. The value of z_0 depends on the slope angle θ. To show the anomaly caused by the hill, we define the measurement zone to be −0.5 to 1.5 km in the x-direction and −1.0 to 1.0 km in the y-direction.

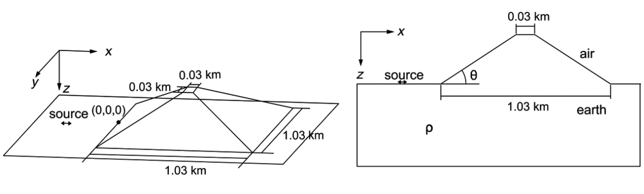

Figure 1. Sketch of the trapezoidal-hill model.

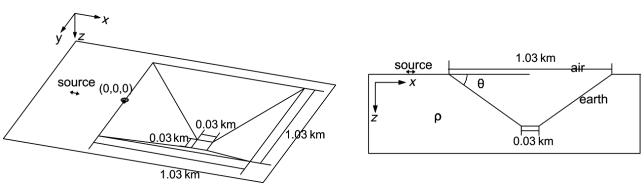

Figure 2. Sketch of the trapezoidal-valley model.

Trapezoidal-valley model

The trapezoidal-valley model is shown in Figure 2. The valley is 0.03 and 1.03 km wide at the base and top. The depth of the base depends on the slope angle. All other parameters are similar to those for the hill model in Figure 1.

3D forward modeling scheme and model mesh description

Data from two models in Figures 1 and 2 have been computed using the 3D CSAMT code presented in Lin et al. (2017). The code models a finite electric dipole as the transmitter. To handle the singularity of the field at the source location, the total EM fields are separated into a primary part and a secondary part, in which the primary part contains the singularity. The arbitrary topography is approximate by steps. The primary EM fields generated by an electric dipole at (or under) the flat surface on either a uniform whole space or a layered half-space is evaluated using the expressions given by Ward and Hohmann (1987).

To calculate the primary fields over the topography, the altitude of the highest point of the true air-earth interface is taken as the altitude of the flat surface. The finite-difference (FD) method is then used to numerically simulate the secondary EM fields at the center of any cell top face at the air-earth interface. Then, the secondary EM fields are interpolated to the arbitrary receiver position using an interpolation vector considering the topography. The total EM fields on the surface are calculated with primary field values evaluated directly at the given receiver location. Using the electric field parallel to the source and the perpendicular magnetic field, the scalar CSAMT apparent resistivity and phase responses can be obtained by the Cagniard equations:

$$\rho_s = \frac{1}{\omega\mu_0}\left|\frac{E}{H}\right|^2, \tag{1}$$

$$\varnothing = \mathrm{Arg}\left(\frac{E}{H}\right), \tag{2}$$

where E is the electric field parallel to the source, H is the magnetic field perpendicular to the source, ω is the angular frequency, μ_0 is the vacuum magnetic permeability, ρ_s is the apparent resistivity, and $\varnothing$ is the phase. The accuracy of the code has been successfully verified by comparing the 3D CSAMT responses at 10 Hz of an elongated cosinusoidal shaped hill with the solutions computed by the 2D adaptive finite-element code by Key and Ovall (2011). More details about the code can be found in Lin et al. (2017).

In this study, we found that the code is not accurate enough to simulate the response over the slope at high frequencies, such as 1000 or 10,000 Hz. The inaccuracy possibly derives from calculating the secondary electric fields at the center of the cell top face at the air-earth interface in the presence of topography. As presented in equation A-14 of Lin et al. (2017), the derivative of the secondary vertical electric fields with respect to x, $(\partial E_{2z}/\partial x)$, can be approximated by two nodal values within volumes with the same medium. This approximation works at low frequencies as shown in Figure 4 in Lin et al. (2017). The deviation (3.8% maximum difference) in the xy mode apparent resistivity over the hill is larger than those on the flat for the model. The deviation becomes larger when the frequency is higher. There are two possible reasons: One is that the position using that approximation to compute $(\partial E_{2z}/\partial x)$ is not at the center of the cell top face; the other is that the interpolation using two nodes is not accurate enough. The current focuses on the shallow part and varies greatly near the air-earth interface at high frequencies. This causes the larger deviations. The numerical instability can be solved by modifying the algorithm using three nodes to calculate the derivatives of the fields as presented in Li et al. (2008). To verify this, the apparent resistivities in XY mode at 1000 and 10 Hz of a 2D hill model is shown in Figure 3. The apparent resistivity (dashed black lines) at 10 Hz calculated by the unmodified code (Lin et al., 2017) match within 4% with those (solid blue lines) computed by the code given by Key and Ovall (2011). However, significant differences are seen at 1000 Hz over the slope. The apparent resistivity with the modified code (red pluses) is in good agreement with the solutions computed by Key and Ovall (2011) at 10 and 1000 Hz. The numerical results of the phase responses (not shown here) show a similar pattern.

Based on the 3D FD code, we discretized the investigated models using a rectangular mesh. The grid around the topography should be as fine as possible to get more accurate data. To obtain a solution with sufficient accuracy, and moderate computation time and memory consumption, the side lengths of the cubes over the slope of all models are kept less than 10% of the skin depth (δ is determined by $\delta = 503\sqrt{\rho/f}$, ρ is the earth resistivity and f is the frequency) at the corresponding frequency. As an example, the mesh for the hill model with a slope angle of 45° at the frequencies $\leq$ 1000 Hz is shown in Figure 4. The side lengths of the cubes over the slope are 10 m, which is less than 10% of the skin depth (159 m) at 1000 Hz. The side lengths of the cubes, in which the topography has abrupt change, are 5 m. The side lengths of the cubes outside the range of the hill in the horizontal direction and from the hill base in the z-direction (not shown in Figure 4) are gradually increased toward the model edges. To satisfy the boundary condition, the longest side lengths at the model edges are approximately 10 times the skin depth. The mesh at the source location is also refined to deal with the source singularity.

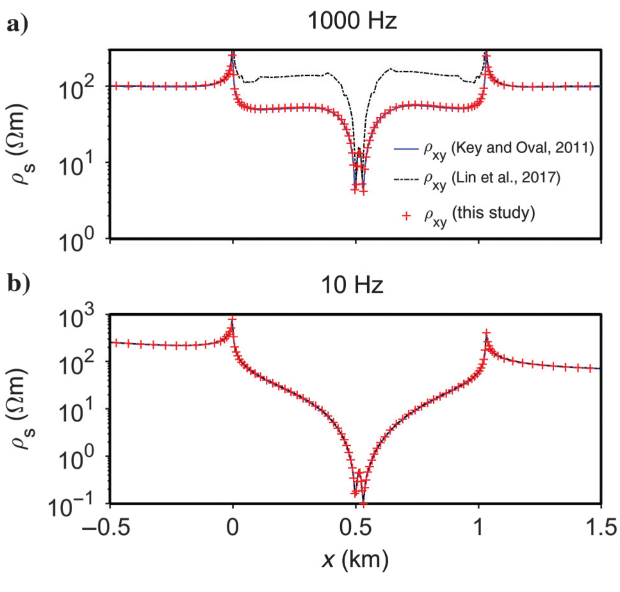

Figure 3. The apparent resistivities in the XY mode at (a) 1000 and (b) 10 Hz of a 2D hill model. The 2D hill model has the same x-z cross section as that of the hill model in Figure 1 with a slope angle of 45°, resistivity of 100 Ωm, and the mesh in Figure 4. The solid blue lines represent the solutions computed using the code by Key and Ovall (2011), the dashed black lines show the results from the unmodified code by Lin et al. (2017), and the red pluses represent the results with the modified code.

3D simulation approach

Table 1 shows the model geometries used to simulate the responses. These parameters give 210 ($6\times5\times7$) unique combinations for each model.

In CSAMT field work, the source and the measurement zone (the zone having receiver positions) are usually separated with a certain distance. For this reason, we consider two cases: one for receivers located in an area of topography and transmitter on a flat surface and the other in which the transmitter is located in an area of topography and receivers on a flat surface. This results in a total of 420 (210×2) combinations. To describe the source effects conveniently, the whole field zone is divided into the near-field, transition-field, and far-field zones. When the measurement zone is far from the source ($r > 4\delta$, where r is the distance between source and receiver, δ is the skin depth), EM fields are in the far-field zone; when it is close to the source ($r < 0.5\delta$), they are in the near-field

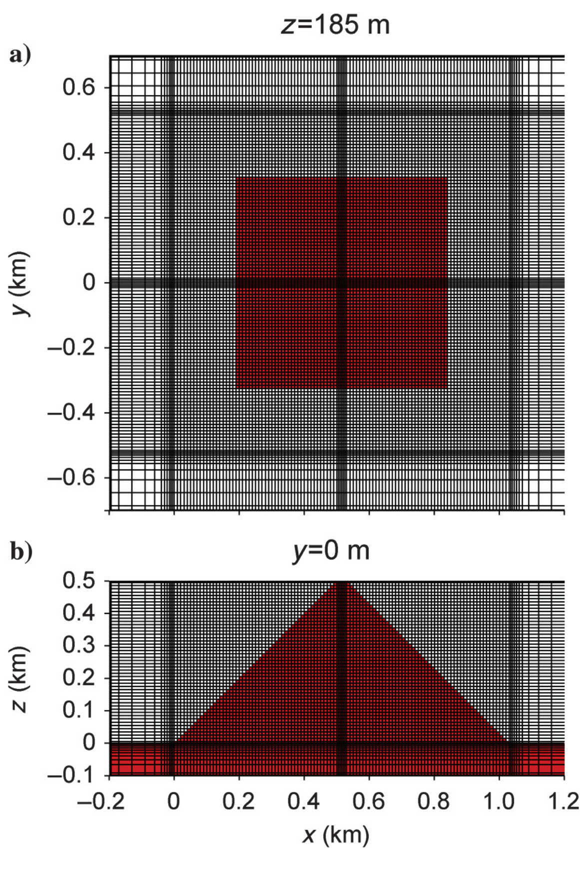

Figure 4. (a) Plan view at $z = 185$ m and (b) cross-section views at $y = 0$ m of the mesh for the hill model with a slope angle of 45° and resistivity of 100 Ωm for frequencies $\leq$ 1000 Hz.

zone; and the remaining area is the transition-field zone (Hughes and Carlson, 1987; Vozoff, 1990; Shlykov and Saraev, 2014).

The corresponding CSAMT apparent resistivity and impedance phase responses for the models are computed using the electric fields and magnetic fields. To highlight the effect on the response of a target, the observed electric field amplitude is usually normalized by the response on a priori background structure (Li and Constable, 2007). Here, we use a half-space with a flat surface as the reference model with the same earth resistivity as the topographic models. The response on the flat surface for the reference models is used to normalize the amplitudes and to subtract from the phases of the responses of the topographical surface. This is done for amplitudes of the electric fields, magnetic fields, and apparent resistivities. We call this the normalized response. It is well-known that

Table 1. The parameters used in the simulation for the two models.

Parameters	Values
f (Hz)	0.1, 1, 10, 100, 1000, and 10,000
ρ (Ωm)	1, 10, 100, 1000, and 10,000
δ (m)	50, 159, 503, 1591, 5030, and 15,906
θ (°)	5, 10, 15, 30, 45, 60, and 75

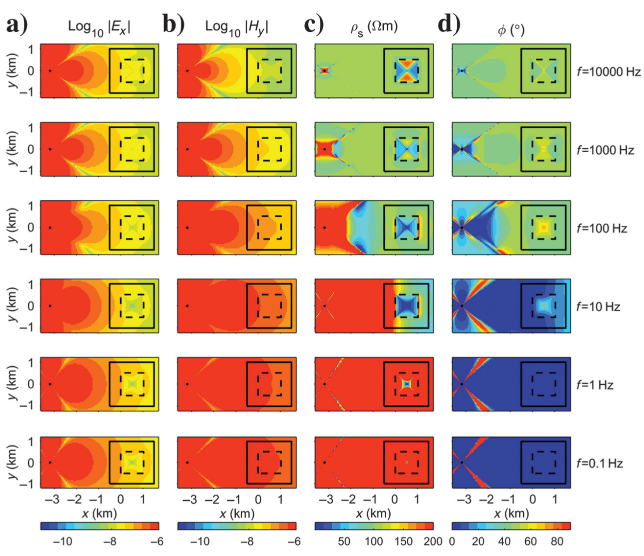

Figure 5. The amplitude of the horizontal electric field (a), horizontal magnetic field (b), apparent resistivity (c), and phase responses (d) at six frequencies ($f = 10{,}000$, 1000, 100, 10, 1, and 0.1 Hz) on the hill model in Figure 1 with a slope angle of 45° and earth resistivity of 100 Ωm. The solid black line rectangle represents the measurement zone (−0.5 to 1.5 km in the x-direction and −1.0 to 1.0 km in the y-direction), the dashed black line rectangle denotes the area of hill (0–1.03 km in the x-direction and −0.515 to 0.515 km in the y-direction), and the black circle shows the position of the transmitter (hill-slope angle of 45° and earth resistivity of 100 Ωm for frequencies of 10,000–0.1 Hz).

CSAMT responses vary with the frequency and earth resistivity similar to MT responses. Our numerical results, however, show that the same skin depth (determined by the frequency and earth resistivity) leads to the same normalized values (or subtracted values for phase) no matter how the frequency or the earth resistivity changes. Hence, it is more convenient to discuss the effects of topography in the far-field and near-field zone using skin depth as a varying parameter. Therefore, the six frequencies and five resistivity values are modified to the six corresponding skin depth values in Table 1. Then, the 420 combinations for each CSAMT response are reduced to 84 ($6 \times 7 \times 2$) combinations for each corresponding normalized (or subtracted) values.

In our simulations, we consider only scalar data, which is currently the most widely used in CSAMT exploration. Only the responses acquired with the axial dipole array (an x-directed dipole source) are shown. Similar results can be obtained with the responses acquired with the equatorial dipole array (a y-directed dipole source), and therefore they are not shown in this paper. Furthermore, we choose 10% as the noise level for field CSAMT data. The distortions caused by topography for the electric field, magnetic field, and apparent resistivity responses of less than 10% can be accepted. The corresponding error level for the impedance phase is 5% (2.86°).

RESPONSES ON MODELS WITH RECEIVERS LOCATED IN AN AREA OF TOPOGRAPHY AND TRANSMITTER ON A FLAT SURFACE

Trapezoidal-hill model

Horizontal electric field responses

Responses are shown in Figure 5, in which Figure 5a shows the amplitude of the horizontal electric field $|E_x|$ at six frequencies on the hill model in Figure 1 with a slope angle of 45° and earth resistivity of 100 Ωm. The $|E_x|$ responses seem to have smaller values over the hill, compared with the background values. However, the responses generated by the hill are mixed with those generated by the source and therefore hardly recognizable.

To highlight the effect of the hill on the responses, the normalized $|E_x|$ in the measurement zone is shown in Figure 6a. The slope angle of the model is still 45°. The $|E_x|$ anomaly is generally low over the hill except for the points over the two slopes in the y-direction and close to the edges, when the receivers are in the far-field zone at the skin depths of 50 and 159 m. The high $|E_x|$ anomaly near the bottom edges of the slopes in the x-direction and the low $|E_x|$ anomaly near the bottom edges of the slopes in the y-direction can also be found in the far-field zone. As the receiver changes from the far-field zone to the near-field zone, the range of the low $|E_x|$ anomaly becomes larger over the hill. In the near-field zone at the skin depths of 5030 and 15,906 m, only the low $|E_x|$ anomaly over the hill and the high $|E_x|$ anomaly near the bottom edges of the slopes in the x-direction are found.

The hill effects depend on the roughness of the surface topography. In Figures 7a and 8a, the normalized $|E_x|$ for seven different slope angles in the near-field zone at the skin depth of 15,906 m and in the far-field zone at the skin depth of 159 m are shown. From these figures, it is clear that the distortions on the $|E_x|$ become more significant as the slope angles increase. The $|E_x|$ effects of the hill for slope angles ≤5° in the near-field and for slope angles ≤15° in the far-field zone seem to be weak enough (less than 10%) and can therefore be neglected.

Horizontal magnetic field responses

The Figure 5b shows the amplitude of the horizontal magnetic field $|H_y|$ at six frequencies on the hill model in Figure 1 with a slope angle of 45° and earth resistivity of 100 Ωm. The $|H_y|$ responses generated by the hill are not recognizable because they are totally mixed with those generated by the source.

The normalized $|H_y|$ for the six skin depths is shown in Figure 6b. The $|H_y|$ anomaly is high over the hill and near the bottom edges of the slopes in the x-direction and low near the bottom edges of the slopes in the y-direction, when the receivers are in the far-field zone at the skin depths of 50 and 159 m. As the receiver changes from the far-field zone to the near-field zone, the low $|H_y|$ anomaly becomes weaker and the high $|H_y|$ anomaly over the hill turns into the low anomaly. In the near-field zone at skin depths of 5030 and 15,906 m, only the weak low $|H_y|$ anomaly over the hill can be found.

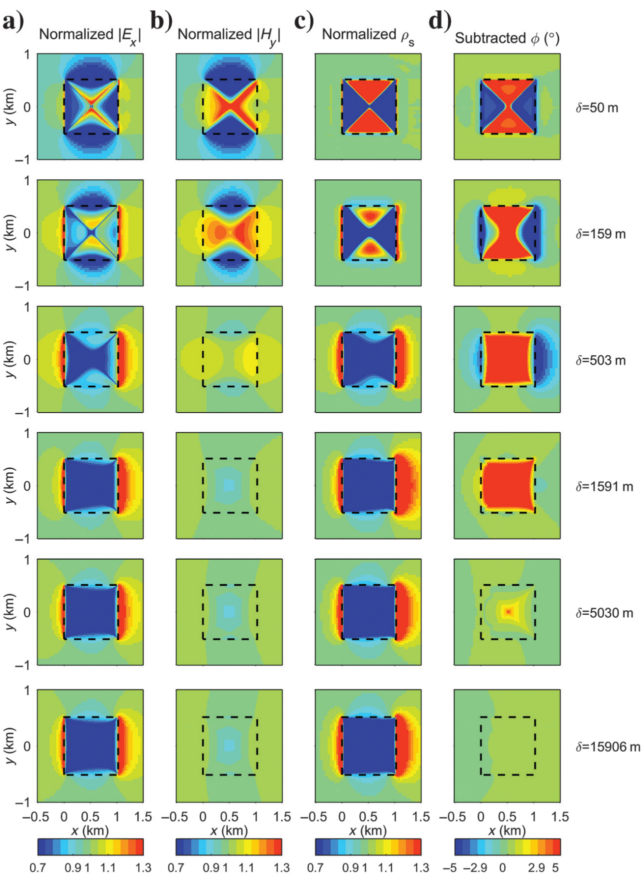

Figure 6. The amplitude of the horizontal electric field (a), horizontal magnetic field (b), apparent resistivity (c) from Figure 5 normalized by the corresponding values of the flat-surface reference model in the measurement zone for six different skin depths ($\delta = 50$, 159, 503, 1591, 5030, and 15,906 m). The phase (d) has been subtracted the phase from the reference model (skin depths from 50 to 15,906 m and hill-slope angle of 45°).

Figures 7b and 8b display the normalized $|H_y|$ for seven different slopes in the near-field zone at the skin depth of 15,906 m and in the far-field zone at the skin depth of 159 m. It is obvious that the distortions on the $|H_y|$ become more significant as the slope angles increase. However, the $|H_y|$ are less affected by the same hill model (same slope angle) than the $|E_x|$. The $|H_y|$ effects of the hill for slope angles ≤45° in the near-field zone and for slope angles ≤10° in the far-field zone seem to be weak enough (less than 10%) and can therefore be ignored.

Apparent resistivity and phase responses

Figure 5c and 5d shows the ρ_s and ϕ responses at the six frequencies on the hill model with a slope angle of 45° and earth resistivity of 100 Ωm. The ρ_s and ϕ responses generated by the hill can be easily differentiated from the background values at high frequencies, 10,000–100 Hz. At low frequencies, 10–0.1 Hz, however, the ρ_s and ϕ responses generated by the hill are

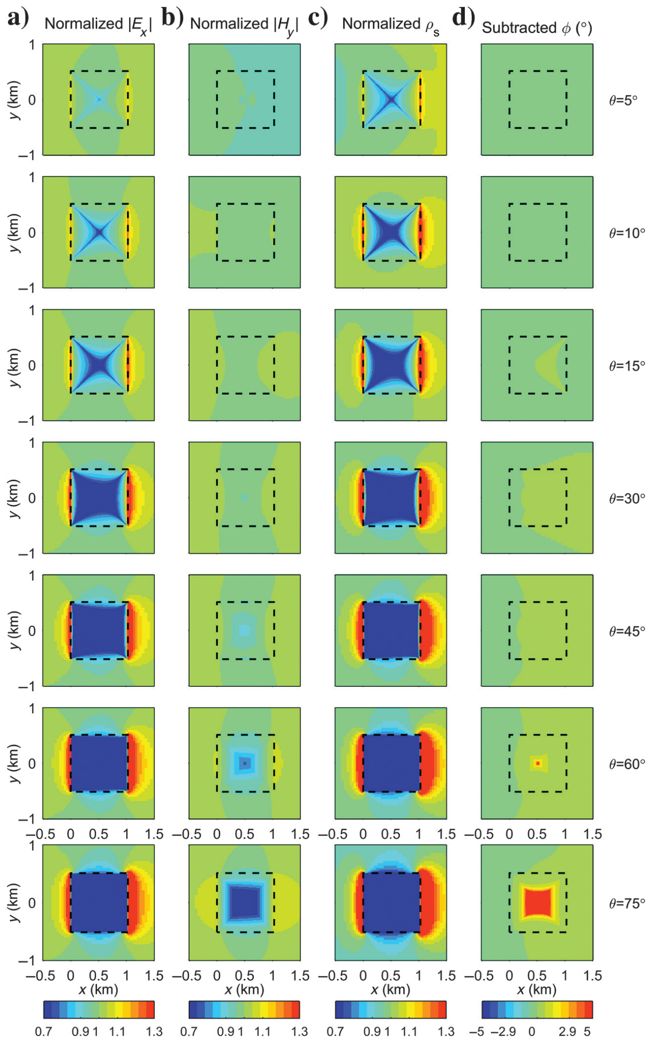

Figure 7. The same as Figure 6, but for a single skin depth of 15,906 m and with seven different hill-slope angles ($\theta = 5°$, 10°, 15°, 30°, 45°, 60°, and 75°) (skin depth of 15,906 m and different hill slopes).

still mixed with those generated by the source and are hardly recognizable.

The normalized ρ_s and ϕ, which make the influence of the hill more prominent, are shown in Figure 6c and 6d. In the x-direction, the ρ_s anomaly is low over the hill top and the two slopes and high near the bottom edges of the slopes, when the receivers are in the far-field zone at the skin depths of 50 and 159 m. This phenomenon is consistent with the 2D TM mode MT results in Wannamaker et al. (1986), the 3D XY-mode MT responses in Nam et al. (2007), and the 3D XY-mode RMT results in Ren et al. (2013) because the CSAMT responses in the far-field zone should be similar to the MT and RMT responses. The drop over the hill and the increase above the valley in apparent resistivity can be explained by the current density decrease on the hill and corresponding focusing in the valley (Jiracek, 1990; Ren et al., 2013). Figure 6a also clearly shows that the electric fields are reduced on hills and increased in valleys in the far-field zones due to the galvanic effects. It is also found that the magnetic fields are increased on the hills. That means the magnetic fields also contribute to the drop in apparent resistivity. In the far-field zone, a high ρ_s anomaly can be found over the two slopes in the y-direction. This high anomaly could be explained by the decreased horizontal magnetic fields over the two slopes (Figure 6b) even if the electric fields are also reduced. This high anomaly is also consistent with the 2D TE mode MT results at 2000 Hz in Wannamaker et al. (1986). As presented in this paper, the horizontal magnetic field anomaly is caused by the total magnetic fields being essentially parallel to the slope because of the high frequencies. Our magnetic field vector plots along the line at $x = 0.515$ km on the hill model prove this description. At frequencies of 10,000 and 1000 Hz, the total magnetic fields are basically parallel to the slope. And at low frequencies of 10–0.1 Hz, the total magnetic fields on the slope are horizontal.

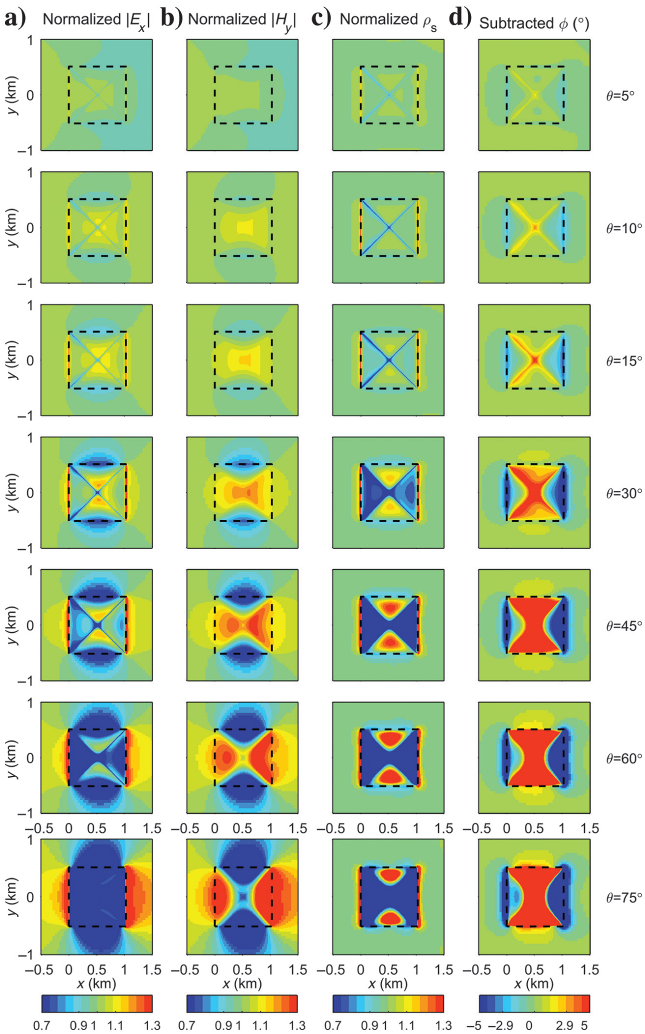

Figure 8. The same as Figure 6, but for a single skin depth of 159 m and with seven different hill-slope angles ($\theta = 5°$, 10°, 15°, 30°, 45°, 60°, and 75°) (skin depth of 159 m and different hill slopes).

In the far-field zone, the ϕ anomaly is high over the hill and low near the bottom edges of the slopes in the x-direction, which is almost opposite to those for the ρ_s. Again, the total magnetic field parallel to the slope at the two high frequencies leads to the high ϕ anomaly over the two slopes in the y-direction as the ρ_s anomaly. These far-field $|E_x|$, $|H_y|$, ρ_s, and ϕ distortions vary with the change of the skin depth.

As the receiver changes from the far-field zone to the near-field zone, the range of the low ρ_s anomaly becomes larger over the hill, whereas there is a stronger high ρ_s anomaly near the bottom edges of the slopes in the x-direction. In the transition zone at the skin depth of 1591 m, there is only a high ϕ anomaly over the hill. In the near-field zone at the skin depths of 5030 and 15,906 m, only a low ρ_s anomaly over the hill and a high ρ_s anomaly near the bottom edges of the slopes in the x-direction are found. In the near-field zone, the high ϕ anomaly over the hill is quite weak. These near-field ρ_s anomalies can be related to the anomalous $|E_x|$ where there are almost no anomalies for $|H_y|$. The near-field ϕ anomalies are also associated with the corresponding electric and magnetic phases. Because of the source effect, the topographic distortions on the field $|E_x|$, $|H_y|$, ρ_s, and ϕ responses in the near-field zone are different from those in the far-field zone. Compared with the responses in far-field zone, it is seen that there are less distortions on the $|H_y|$ and ϕ data, but there are more distortions on the $|E_x|$ and ρ_s data in the near-field zone. Due to the current density generated by the source in the x-direction, the boundary charges on the two slope edges in the x-direction may be stronger in the near-field zone, leading to the greater reduced electric fields over the hill and the greater increased electric fields in the valley.

Figures 7c, 7d, 8c, and 8d show the normalized ρ_s and ϕ for seven different slope angles in the near-field zone at a skin depth of 15,906 m and in the far-field zone at a skin depth of 159 m. It is found that the topographic distortions on the ρ_s responses are similar to those on the $|E_x|$ responses, whereas the effects on the ϕ responses are somewhat like those on the $|H_y|$ responses. The ρ_s effects of the hill for slope angles ≤10° in the far-field and slope angles <5° near-field zone seem to be weak enough (<10%) and therefore can be ignored. The slope angles with which the ϕ distortions (<2.86°) of the hill in the far-field and near-field zones can be neglected are ≤10° and 45°, respectively.

From a practical point of view, the 50–100 m long dipoles make it nearly impossible to measure the true horizontal electric fields unless one of the electrodes are dug deep into the earth, whereas it is easy to measure the tangential electric fields on a steep slope.

For comparison, the amplitude of the electric fields parallel to the slope ($|E_t|$) and the corresponding apparent resistivities are shown in Figure 9. As shown by the electric field vector plots (Figure 10a and 10b) along the line at $y = 0$ km on the hill model with a slope angle of 45°, the total electric fields on the slope are essentially parallel to the slope and there are no electric fields perpendicular to the slope for any of the six frequencies. The amplitude of the electric fields parallel to the slope can easily be calculated by the horizontal electric fields and the slope angles: $|E_t| = |E_x|/\cos\theta$. Conversely, it is easy to measure truly horizontal magnetic fields because the induction coil sensors can be leveled during the burying. Then, the corresponding apparent resistivities ρ_{st} are computed by the electric fields parallel to slope $|E_t|$ and the $|H_y|$. Compared with the horizontal electric fields and the apparent resistivities in Figure 6, the electric fields parallel to the slope and the corresponding apparent resistivities are less distorted over the two slopes in the x-direction.

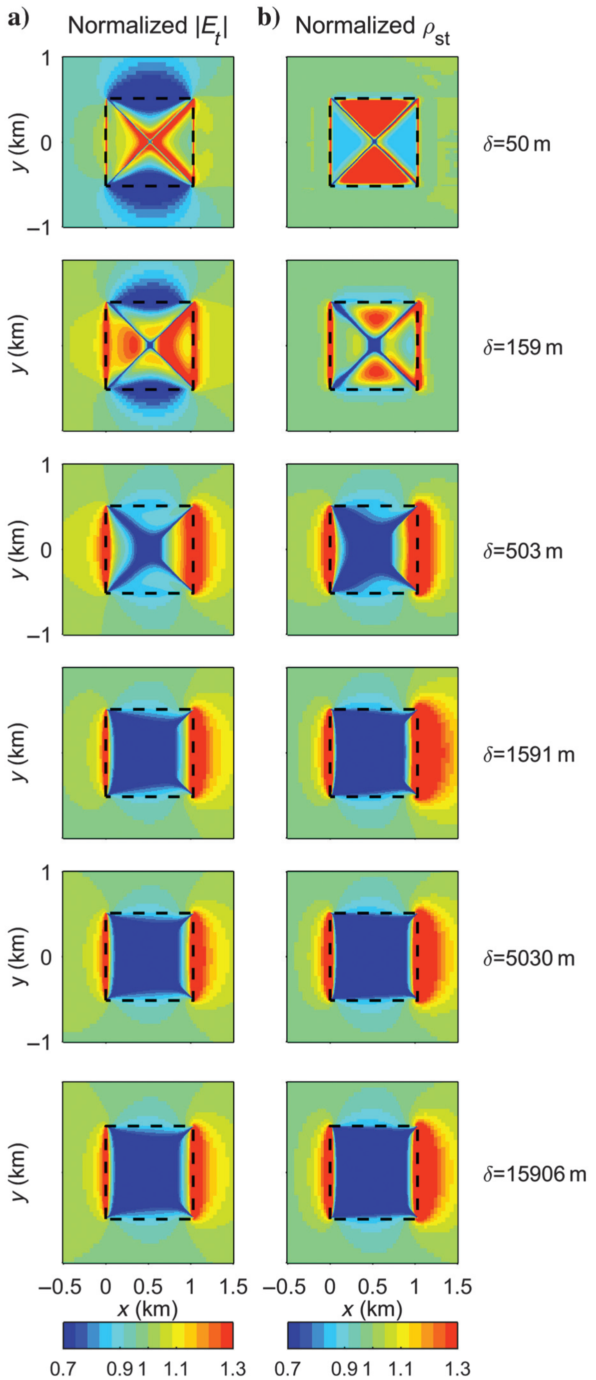

Figure 9. The same as Figure 6, but for the amplitude of the electric fields parallel to the slope (a) and the corresponding apparent resistivity (b) responses (skin depths from 50 to 15,906 m and hill-slope angle of 45°).

Trapezoidal-valley model

The $|E_x|$, $|H_y|$, ρ_s, and ϕ responses and their corresponding normalized values at the six frequencies on the valley model in Figure 2 with a slope angle of 45° and earth resistivity of 100 Ωm are not shown here. In the measurement zone, however, the $|E_x|$, ρ_s, and ϕ responses generated by the valley seem to have the opposite results to those generated by the hill, whereas the $|H_y|$ responses seem to have the similar results.

In Figures 11 and 12, the normalized $|E_x|$, $|H_y|$, ρ_s, and ϕ for seven different slope angles in the near-field zone at the skin depth of 15,906 m and in the far-field zone at the skin depth of 159 m are

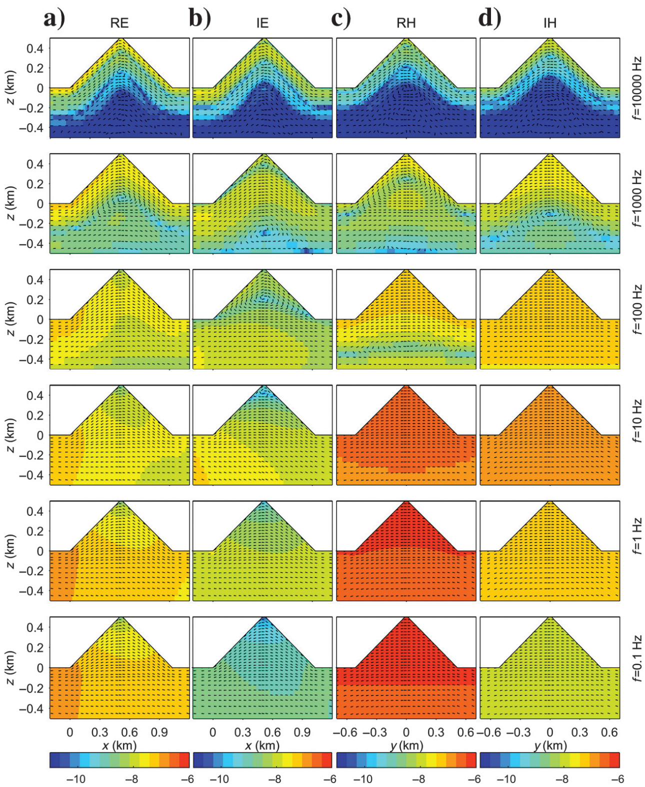

Figure 10. The electric field vector plots (a and b) in vertical sections along the line at $y = 0$ km and the magnetic field vector plots (c and d) along the line at $x = 0.515$ km at the six frequencies ($f = 10{,}000$, 1000, 100, 10, 1, and 0.1 Hz) on the hill model with a slope angle of 45° and earth resistivity of 100 Ωm. RE and IE denote the real and imaginary part of the electric fields, whereas RH and IH denote the real and imaginary part of the magnetic fields, respectively. The amplitudes of the fields are shown in different colors (frequencies from 10,000 to 0.1 Hz and hill-slope angle of 45°).

displayed. It is obvious that the distortion of the valley becomes more significant as the slope angle increases.

In the far-field zone, the effects of the valley are almost opposite to those of the hill, except for $|E_x|$ and ρ_s over the two slopes in the x-direction and ρ_s and ϕ over the two slopes in the y-direction for slope angles $\geq 30°$. The possible reason could be that the dimension of the hill-top/valley-base is much smaller than that of the four slopes. When the slope angles are more than 30°, the reduced/increased electric fields on the hill-top/valley-base are not obvious, compared with those on the four slopes, which are the same for the hill and the valley. Figure 13 shows the electric field vector plots in vertical sections along the line at $y = 0$ km and the magnetic field vector plots along the line at $x = 0.515$ km at the 1000 and 10 Hz on the valley model. Again, the total electric fields are essentially parallel to the valley slope at high and low frequencies, whereas the total magnetic fields are generally parallel to the slope at high frequency, but horizontal at low frequency. The far-field ρ_s and ϕ anomalies over the two slopes in the y-direction are also caused by using the horizontal magnetic fields at high frequencies.

In the near-field zone, the effects of the valley on $|E_x|$ and ρ_s are opposite to those of the hill except for those over the two slopes in the x-direction when the slope angles are more than 30°, whereas the distortions of valley on $|H_y|$ and ϕ are similar to those of the hill. The slope angles with which the $|E_x|$ $|H_y|$, ρ_s, and ϕ distortions of the valley in the near-field zone can be neglected are $\leq 5°$, 45°, 5°, and 60°, respectively. The slope angles with which the $|E_x|$ $|H_y|$, ρ_s, and ϕ distortions of valley in the far-field zone can be ignored are $\leq 10°$.

RESPONSES ON MODELS WITH TRANSMITTER LOCATED IN AN AREA OF TOPOGRAPHY AND RECEIVERS ON A FLAT SURFACE

The above discussion shows the effect of topography when the receiver is located in an area of topography and the transmitter is on a flat surface. The conventional 2D or 3D interpretation of CSAMT data is based on this case, which often neglects the topography near the source if any. However, what happens if the transmitter is located in an area of extreme topography? The importance of account-

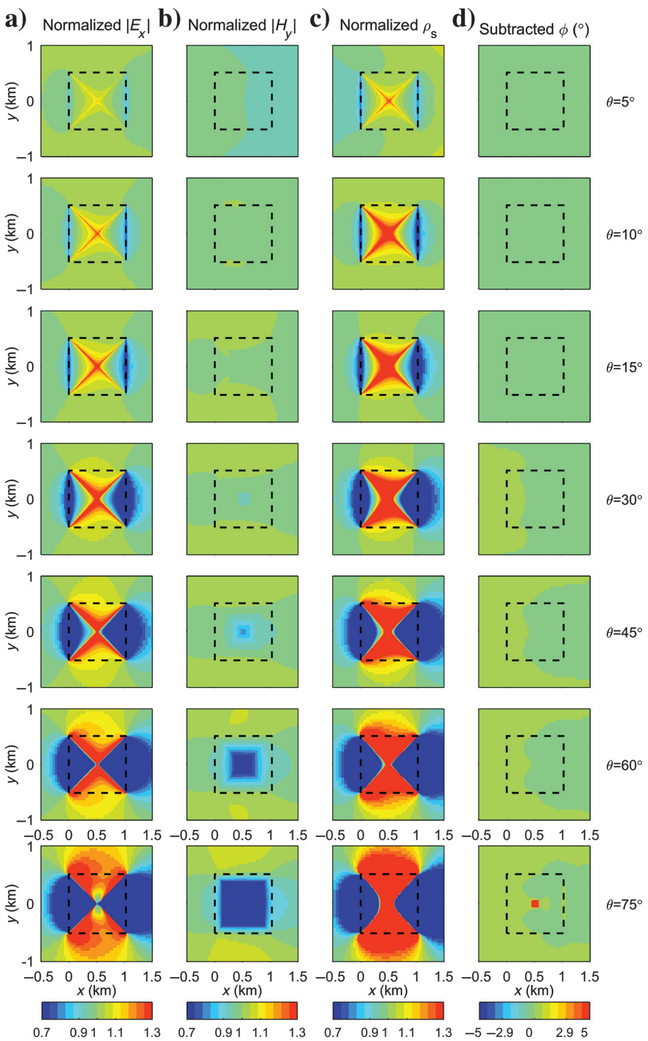

Figure 11. Same as Figure 7, but for the valley model in Figure 2 (skin depth of 15,906 m and different valley slopes).

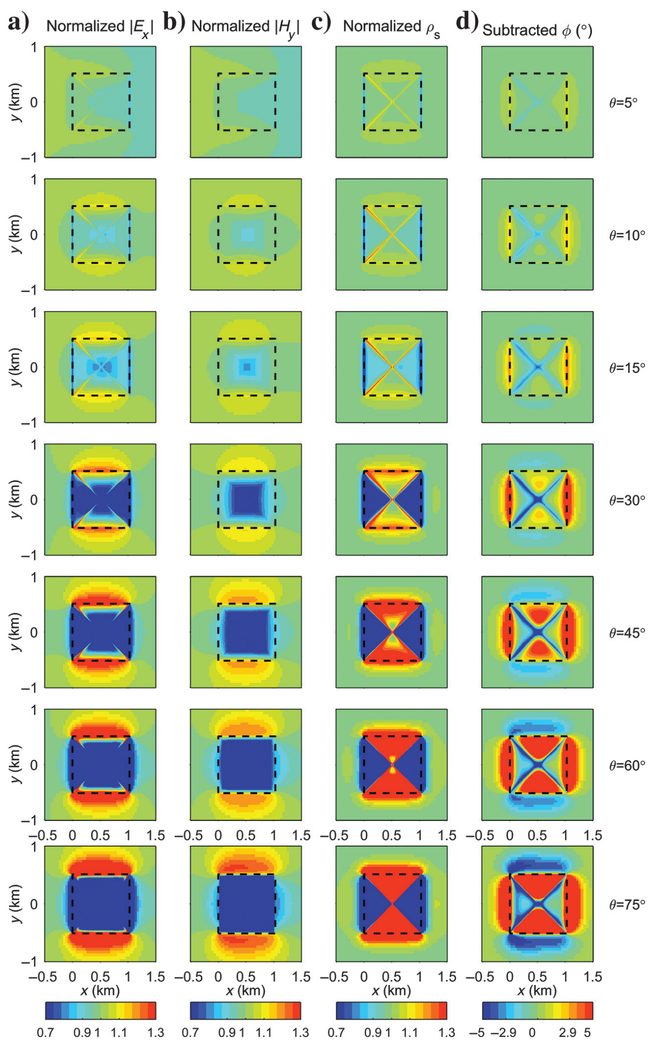

Figure 12. Same as Figure 8, but for the valley model in Figure 2 (skin depth of 159 m and different valley slopes).

ing for the effects of source in an area of topography is shown by the following examples.

Trapezoidal-hill model

A similar hill model as shown in Figure 1 is used except that the range in the x-direction of the hill is changed from −3.7 to −2.57 km. An x-directed HED transmitter is located at (−3.185, 0, $-z_0$) km on the hilltop. The range of the measurement zone is still defined as −0.5 to 1.5 km in the x-direction and −1.0 to 1.0 km in the y-direction. The other parameters used for simulation are the same as those for the model in Figure 1.

Figure 14 shows the amplitude of the $|E_x|$, $|H_y|$, ρ_s, and ϕ at the six frequencies on the hill model with a source on the hilltop, a slope angle of 45°, and earth resistivity of 100 Ωm. In the measurement zone, the $|E_x|$, $|H_y|$, ρ_s, and ϕ responses generated by the hill seem to have no anomaly at any frequencies because they are mixed with those generated by the source and therefore are difficult to differentiate.

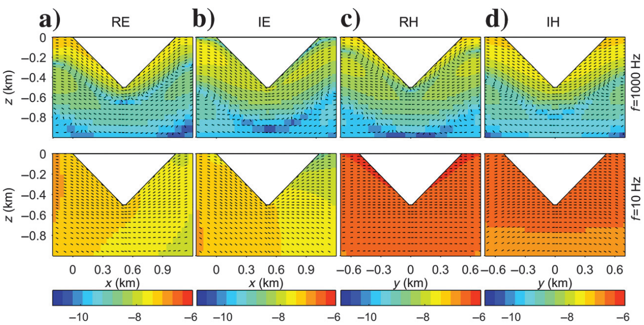

Figure 13. The same as Figure 10, but for the valley model with a slope angle of 45° on and earth resistivity of 100 Ωm at the two frequencies of 1000 and 10 Hz (frequencies at 1000 and 10 Hz and valley slope angle of 45°).

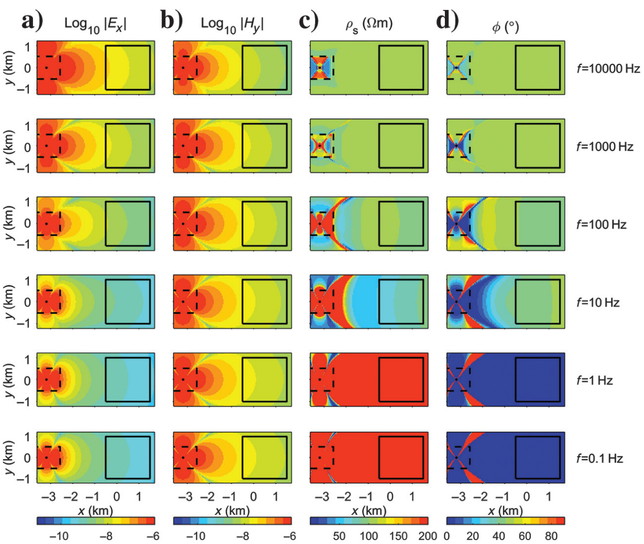

Figure 14. Same as Figure 5, but for the hill model with a source on the hilltop. The dashed black line rectangle denotes the area of hill (−3.7 to −2.57 km in the x-direction and −0.515 to 0.515 km in the y-direction) (hill-slope angle of 45° and earth resistivity of 100 Ωm for frequencies of 10,000–0.1 Hz).

To highlight the hill effects, the normalized $|E_x|$, $|H_y|$, ρ_s, and ϕ are shown in Figure 15. Figure 15 clearly shows that a hill beneath the source generates strong distortions in the near-field zone and the transition zone. In the far-field zone, there are no distortions, which may lead to the impression that the topography has no effect on the response generated in the far-field zone. Similar results were obtained by Lin et al. (2017). However, this picture only displays the result from the hill with the slope angle of 45°. In Figures 16 and 17, the normalized $|E_x|$, $|H_y|$, ρ_s, and ϕ for the seven different slope angles in the near-field zone at the skin depth of 15,906 m and in the far-field zone at the skin depth of 159 m are shown. A strong hill effect is seen for the models with slope angles >30° in Figure 16. In Figure 17, however, strong hill distortion in the far-field zone can also be found on the models with slope angles of 60° and 75°. This observation is in good agreement with the analysis of the source-overprint effect (Lei et al., 2016, Figure 5), showing that the CSAMT apparent resistivity data in the far-field zone are also greatly affected by a low-resistivity body beneath the source. From this point of view, our previous conclusion that the distortion generated by the topography at the source position can be neglected when the receiver is far away from the source (Lin et al., 2017) is not valid. Compared with the responses in the far-field zone, the responses in the near-field zone are more easily affected by the hill beneath the source. The distortions generated by the hill beneath the source in the near-field zone and in the far-field zone

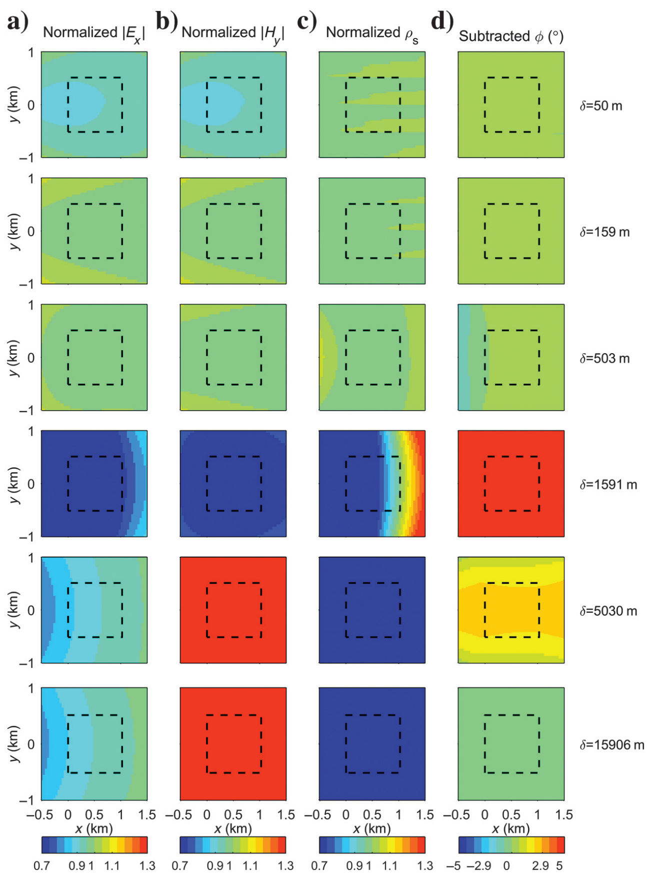

Figure 15. The same as Figure 6, but for the hill model with a source on the hilltop (skin depths from 50 to 15,906 m and hill-slope angle of 45°).

can be explained by source-overprint effect (Zonge and Hughes, 1991; Lei et al., 2016). If we compare the responses affected by the hill in the survey area (Figures 6–8) to those at the source position (Figures 15–17), the CSAMT responses seem to be more sensitive to the topography in the survey area than that at the source position. The hills with small slope angles (5° and 10°) in the survey area can cause strong distortions, whereas only the hills with large slope angles (≥30°) at the source position generate strong effects.

Trapezoidal-valley model

A similar valley model as shown in Figure 2 is used except for the range in the x-direction of the valley, which is changed from −3.7 to −2.57 km. An x-oriented HED transmitter is located at (−3.185, 0, z_0) km on the valley base. The range of the measurement zone is still defined as −0.5 to 1.5 km in the x-direction and −1.0 to 1.0 km in the y-direction.

The $|E_x|$, $|H_y|$, ρ_s, and ϕ responses and their corresponding normalized values on the valley model with a source on the valley base with a slope angle of 45° and earth resistivity of 100 Ωm are not shown here. With this valley slope angle, however, there are almost no (or very weak) distortions in the near- and far-field zones. Some relatively stronger distortions on ρ_s and ϕ data is only found in the transition zone at the skin depth of 1591 m, but the deviations are less than 8%.

Figures 18 and 19 show the normalized $|E_x|$, $|H_y|$, ρ_s, and ϕ for seven different slope angles in the near-field zone at the skin depth of 15,906 m and in the far-field zone at the skin depth of 159 m. We can also see the weak valley effects for all the models in the near- and the far-field zones. Some relatively stronger distortions on the ρ_s data in the near-field zone can be found on the models with slope angles of 60° and 75°, but the deviations are also less than 8%. This also implicates that the responses in the near-field zone are more easily affected by the valley at the source position than those in the far-field zone. If we compare the responses affected by the hill at source position (Figures 16 and 17) to those by the valley (Figures 18 and 19), CSAMT responses seem to be more sensitive to the hill than the valley at the source position. The possible reason is that the hill beneath the source causes the wave stratum to attenuate

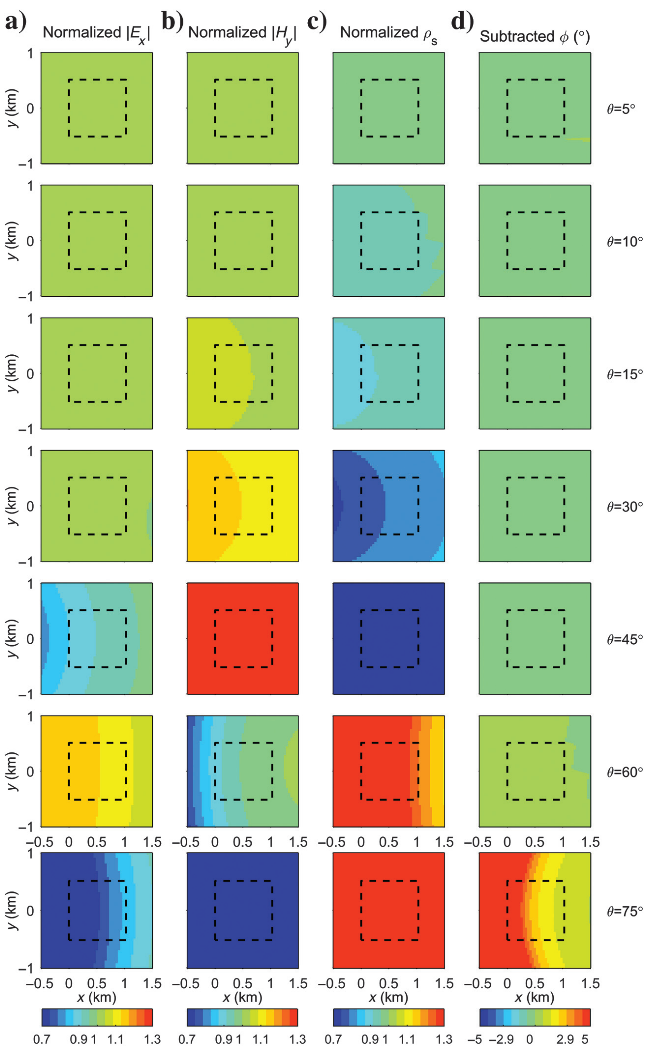

Figure 16. The same as Figure 7, but for the hill model with a source on the hilltop (skin depth of 15,906 m and different hill slopes).

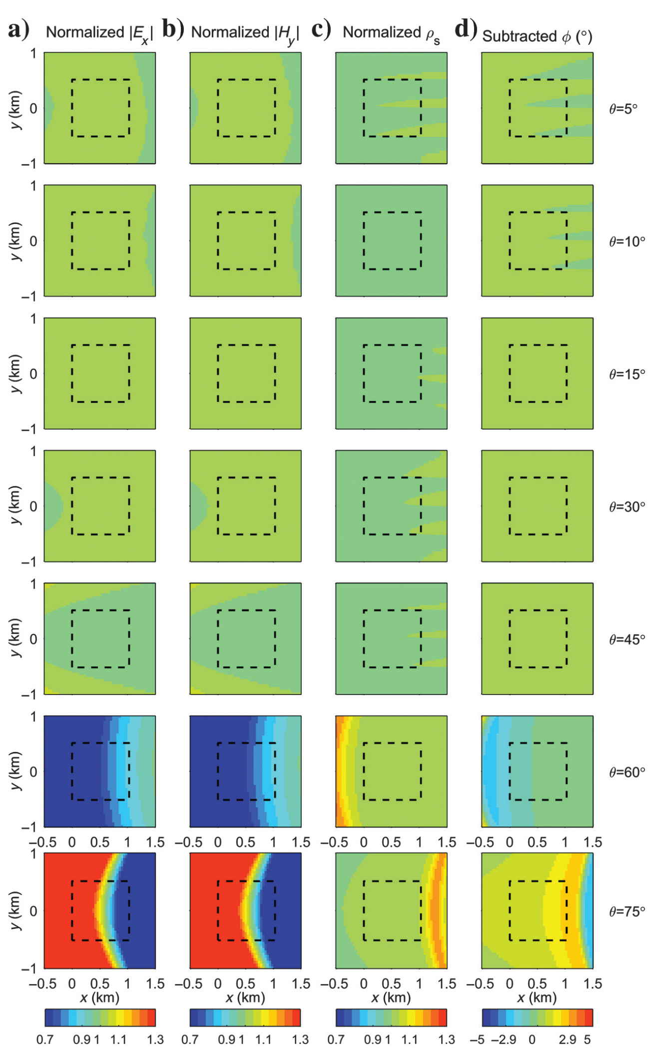

Figure 17. The same as Figure 8, but for the hill model with a source on the hilltop (skin depth of 159 m and different hill slopes).

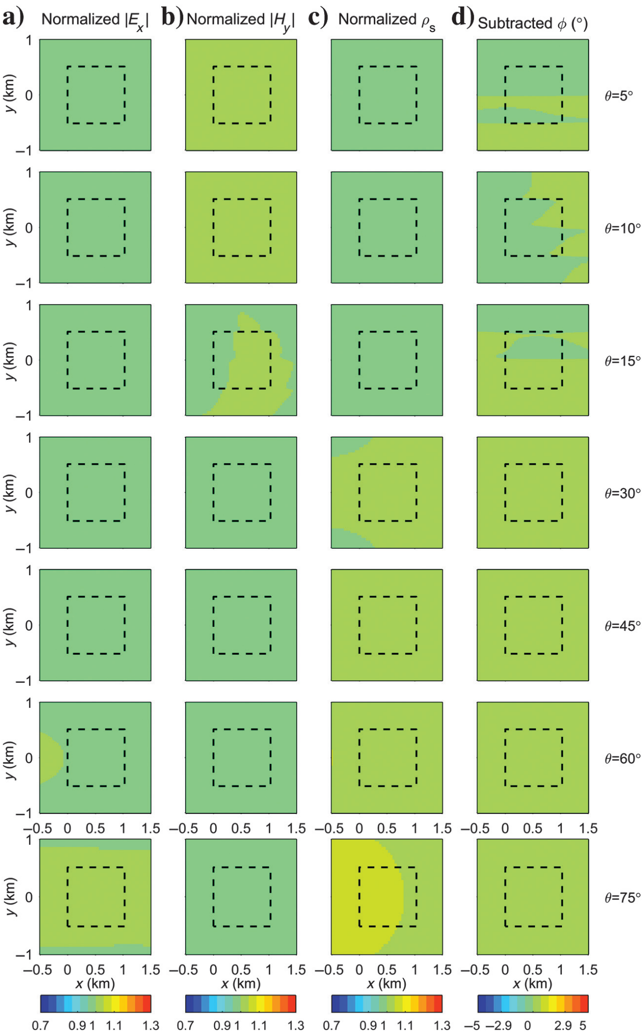

Figure 18. The same as Figure 7, but for the valley model with a source on the valley base (skin depth of 15,906 m and different valley slopes).

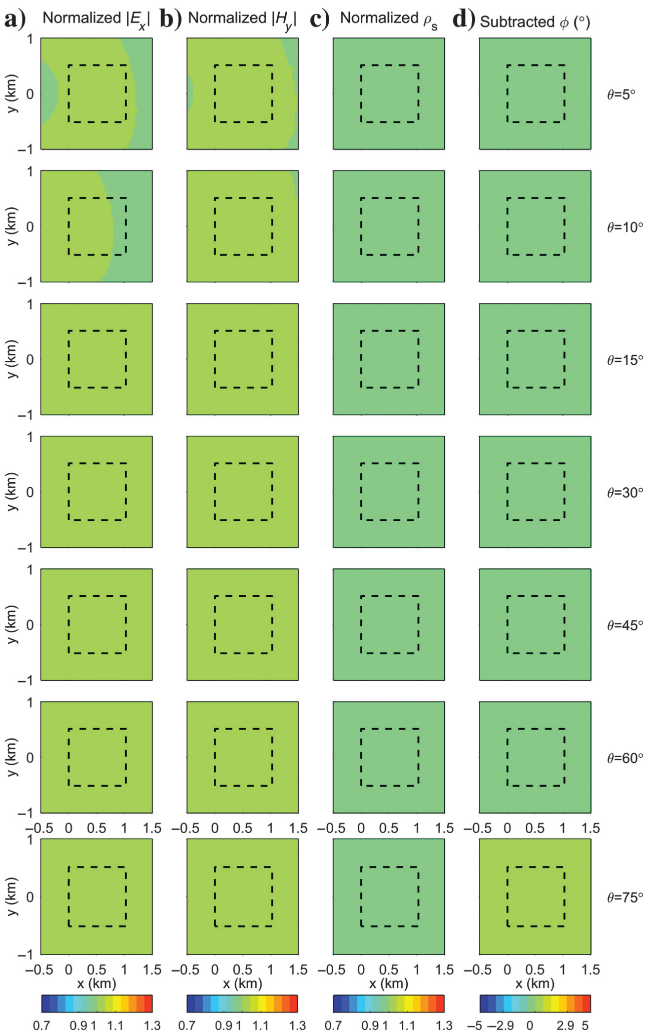

Figure 19. The same as Figure 8, but for the valley model with a source on the valley base (skin depth of 159 m and different valley slopes).

more rapidly than the valley does, leading to the more pronounced effect of source overprint on the data for the hill.

CONCLUSION

The results of the numerical experiments for the 3D trapezoidal models show that the CSAMT $|E|$, $|H|$, ρ_s, and ϕ responses are distorted by the 3D undulated terrain, but to different extents. The effects of 3D topography on CSAMT responses depend on the transmission-receiver-topography geometry, the transmission frequency, earth resistivity, and the roughness of land-surface topography.

The results demonstrate that CSAMT responses are strongly distorted not only by the 3D topography (hill and valley) in the survey area, but also by the 3D topography (hill) at the source position. Therefore, the topography in the measurement area and near (or at) the source location should be accounted for in the inversion or interpretation of CSAMT field data sets.

When the receiver is located in an area of topography and transmitter located on a flat surface, the effects on the hill model and the valley model are examined. Due to the source effect, the effects of 3D topography on the CSAMT $|E|$, $|H|$, ρ_s, and ϕ responses in the near-field zone are quite different from those in the far-field zone, which are similar to the MT or RMT. The CSAMT responses in the near-field zone are less distorted in the $|H|$ and ϕ, but more distorted on the $|E|$ and ρ_s over the hill and valley, compared with those in far-field zone. The topographic distortions of the four CSAMT responses are different from each other. These differences are complicated and vary with the skin depth and the roughness of surface topography. However, there are some common features. All these distortions on CSAMT $|E|$, $|H|$, ρ_s, and ϕ responses become stronger as the roughness increases in the near- and far-field zones. The effects generated by the topography on the ρ_s are similar to those on the $|E|$, whereas the topographic distortions on the ϕ are somewhat like those on the $|H|$. Furthermore, we examined the roughness with which the topographic distortion can be neglected if the noise level is defined as 10%. In the far-field zone, the slope angles with which the $|E|$, $|H|$, ρ_s, and ϕ distortions of hill and valley can be ignored are $\leq 10°$. In the near field, however, the slope angles with which the distortions can be neglected are different between hill and valley among the four different responses.

When the receiver is located on a flat surface and the transmitter is located on the hill, strong topographic distortions can also be found in the near- and far-field zones due to the source-overprint effect. A hill beneath the source can generate significant distortions even in the far-field zone, whereas a valley at the source position causes much weaker distortions (<8%) that can be neglected in the far- and near-field zones. The CSAMT responses seem less sensitive to the topography (hill and valley) at the source position, compared with that in the survey area. Compared with the distortions in the far-field zone generated by the topography (hill and valley) at the source position, those in the near-field zone are relatively stronger.

ACKNOWLEDGMENTS

This study has been jointly supported by the National Key Research and Development Program of China (nos. 2016YFC0601104, 2017YFC0602204), National Natural Science Foundation of China (no. 41674134), the Special Fund for Basic Scientific Research of Central Colleges, Beijing Higher Education Young Elite Teacher Project, and the State Scholarship Fund of China. Constructive comments by C. Farquharson, an anonymous referee and the associate editor E. Slob significantly improved this manuscript and are greatly appreciated.

REFERENCES

Baba, K., and N. Seama, 2002, A new technique for the incorporation of seafloor topography in electromagnetic modeling: Geophysical Journal International, **150**, 392–402, doi: 10.1046/j.1365-246X.2002.01673.x.

Commer, M., and G. A. Newman, 2007, 3D CSEM modeling and inversion for hydrocarbon reservoir mapping: The bathymetry problem: 77th Annual International Meeting, SEG, Expanded Abstracts, 452–456.

Fischer, G., 1989, A strong topographic valley effect in AMT and VLF-R measurements: Geophysical Journal International, **96**, 469–475, doi: 10.1111/j.1365-246X.1989.tb06008.x.

Goldstein, M. A., and D. W. Strangway, 1975, Audio-frequency magnetotellurics with a grounded electric dipole source: Geophysics, **40**, 669–683, doi: 10.1190/1.1440558.

Hoversten, G. M., G. A. Newman, N. Geier, and G. Flanagan, 2006, 3D modeling of a deepwater EM exploration survey: Geophysics, **71**, no. 5, G239–G248, doi: 10.1190/1.2240113.

Hughes, L. J., and N. R. Carlson, 1987, Structure mapping at Trap Spring Oilfield, Nevada, using controlled-source magnetotellurics: First Break, **5**, 403–418, doi: 10.3997/1365-2397.1987021.

Jiracek, G. R., 1990, Near-surface and topographic distortions in electromagnetic induction: Surveys in Geophysics, **11**, 163–203, doi: 10.1007/BF01901659.

Key, K., and J. Ovall, 2011, A parallel goal-oriented adaptive finite element method for 2.5-D electromagnetic modeling: Geophysical Journal International, **186**, 137–154, doi: 10.1111/j.1365-246X.2011.05025.x.

Lei, D., X. Wu, Q. Di, G. Wang, X. Lv, R. Wang, J. Yang, and M. Yue, 2016, Modeling and analysis of CSAMT field source effect and its characteristics: Journal of Geophysics and Engineering, **13**, 49–58, doi: 10.1088/1742-2132/13/1/49.

Li, S., J. R. Booker, and C. Aprea, 2008, Inversion of magnetotelluric data in the presence of strong bathymetry/topography: Geophysical Prospecting, **56**, 259–268, doi: 10.1111/j.1365-2478.2007.00677.x.

Li, Y., and S. Constable, 2007, 2D marine controlled-source electromagnetic modeling. Part 2: The effect of bathymetry: Geophysics, **72**, no. 2, WA63–WA71, doi: 10.1190/1.2430647.

Lin, C., H. Tan, W. Wang, T. Tong, M. Peng, M. Wang, and W. Zeng, 2017, Three-dimensional inversion of CSAMT data in the presence of topography: Exploration Geophysics, doi: 10.1071/EG16067.

Lu, X., M. Unsworth, and J. Booker, 1999, Rapid relaxation inversion of CSAMT data: Geophysical Journal International, **138**, 381–392, doi: 10.1046/j.1365-246X.1999.00871.x.

Mitsuhata, Y., 2000, 2-D electromagnetic modeling by finite-element method with a dipole source and topography: Geophysics, **65**, 465–475, doi: 10.1190/1.1444740.

Nam, M. J., H. J. Kim, Y. Song, T. J. Lee, J. S. Son, and J. H. Suh, 2007, 3D magnetotelluric modeling including surface topography: Geophysical Prospecting, **55**, 277–287, doi: 10.1111/j.1365-2478.2007.00614.x.

Ren, Z., T. Kalscheuer, S. Greenhalgh, and H. Maurer, 2013, Boundary element solutions for broad-band 3-D geo-electromagnetic problems accelerated by an adaptive multilevel fast multipole method: Geophysical Journal International, **192**, 473–499, doi: 10.1093/gji/ggs043.

Sasaki, Y., 2011, Bathymetric effects and corrections in marine CSEM data: Geophysics, **76**, no. 3, F139–F146, doi: 10.1190/1.3552705.

Schwalenberg, K., and R. N. Edwards, 2004, The effect of seafloor topography on magnetotelluric fields: An analytical formulation confirmed with numerical results: Geophysical Journal International, **159**, 607–621, doi: 10.1111/j.1365-246X.2004.02280.x.

Shlykov, A. A., and A. K. Saraev, 2014, Wave effects in the field of a high-frequency horizontal electric dipole: Izvestiya, Physics of the Solid Earth, **50**, 249–262, doi: 10.1134/S1069351314020104.

Vozoff, K., 1990, Magnetotellurics: Principles and practice: Proceedings of the Indian Academy of Sciences — Earth and Planetary Sciences, **99**, 441–471.

Wannamaker, P., J. Stodt, and L. Rijo, 1986, Two-dimensional topographic responses in magnetotellurics modeled using finite elements: Geophysics, **51**, 2131–2144, doi: 10.1190/1.1442065.

Ward, S. H., and G. W. Hohmann, 1987, 4. Electromagnetic theory for geophysical applications, *in* M. N. Nabighian, and J. D. Corbett, eds., Electromagnetic methods in applied geophysics — Theory: SEG, 131–312.

Wirianto, M., W. Mulder, and E. Slob, 2011, Exploiting the airwave for time-lapse reservoir monitoring with CSEM on land: Geophysics, **76**, no. 3, A15–A19, doi: 10.1190/1.3560157.

Zonge, K., and L. Hughes, 1991, 9. Controlled source audio-frequency magnetotellurics, *in* M. N. Nabighian, and J. D. Corbett, eds., Electromagnetic methods in applied geophysics: Applications Part A and Part B: SEG, 713–810.